JMEPEG (2006) 15:23-31
DOI: 10.1361/105994906X83385
©ASM International
1059-9495/$19.00

Laser Welding of 3 mm Thick Laser-Cut AISI 304 Stainless Steel Sheet

Harish Kumar, P. Ganesh, Rakesh Kaul, B. Tirumala Rao, Pragya Tiwari, Ranjeet Brajpuriya, S.M. Chaudhari, and A.K. Nath

(Submitted November 11, 2004; in revised form August 14, 2005)

The objective of the present work was to study the laser weldability of laser-cut 3 mm thick AISI 304 austenitic stainless steel sheet (using oxygen as an assist gas). For minimizing heat input during laser cutting, which is an important factor influencing the thickness of the oxide layer on the cut surface, laser cutting was performed in pulsed mode. The results of the study demonstrated that although the laser welding of laser-cut specimens did not result in the formation of weld defects, the resultant laser weldments exhibited reduced ductility with respect to base metal and bead-on-plate laser weldments. Laser-cut and laser-welded specimens also displayed higher notch sensitivity than the base metal. However, laser-cut and laser-welded specimens still possessed enough ductility to pass guided bend tests.

Keywords austenitic stainless steel, CO_2 laser, laser cutting, laser welding

1. Introduction

High-power CO_2 lasers are finding extensive industrial application in metal sheet cutting. Cutting with a laser beam (LB), a highly focused source of energy, offers a high degree of precision, a narrow kerf width, a low roughness of the cut surfaces, and a minimum heat-affected zone. A laser, integrated with a computer-controlled workstation, facilitates the easy cutting of complex shapes. Often, laser-cut sheets are required to be welded. Nielsen and Broden (Ref 1) studied the weldability of laser-cut austenitic stainless steel (ASS) sheets with gas tungsten arc welding. He reported that stainless steel (SS) sheets, laser-cut with 100% oxygen, were not weldable. On the other hand, SS sheets, cut with a gas mixture of 60% helium and 40% oxygen, produced sound welds. But laser cutting with the gas mixture brought about a 25% reduction in the cutting speed (Ref 1). The work did not address mechanical property characterization of the resultant welds. The present work was undertaken with the objective of studying the laser weldability of laser-cut 3 mm thick AISI 304 ASS sheets using oxygen as the cutting gas, and to characterize the microstructural and mechanical properties of the resultant weldment.

2. Background

The laser cutting of metal sheets is carried out by scanning the surface of the sheets with a focused LB while subjecting the irradiated metal to a high-pressure gas jet coming out of the cutting nozzle. For laser cutting, the focal point of the LB is set very close to the nozzle opening. The mechanism of laser cutting involves the rapid laser melting and blowing out of molten metal with a high-pressure gas jet. Laser-cutting efficiency in ferrous materials is enhanced by using oxygen as an assist gas. The use of oxygen during laser cutting provides an additional heat source in the form of an exothermic reaction involving the oxidation of iron, and so the formed iron oxide, by virtue of its low adherence, is easily blown out of the cut front. In the laser cutting of mild steel sheets, 60 to 70% of the total energy requirement is met by the oxidation energy (Ref 2). The use of oxygen thus facilitates cutting at higher speeds. Ivarson et al. (Ref 3, 4) reported that in the laser cutting of mild steel, about 50% of the ejected iron gets oxidized. FeO is the major constituent (97.6 mol.%) of the ejected oxides, while Fe_2O_3 accounts for the rest (2.4 mol.%). The oxidation reaction involved in the formation of FeO is as follows:

$$Fe + 1/2\ O_2 \rightarrow FeO \qquad \Delta H = -257.58\ kJ/mol \text{ at } 2000\ K \text{ (Ref 5)}$$

The laser cutting of ASS sheets is usually carried out with either oxygen or an inert gas. Oxygen-assisted cutting is the more common method. The use of oxygen in cutting SS sheet involves the formation of refractory chromium oxide (melting temperature 2453 K), which poses difficulty in its efficient ejection from the cut front (Ref 6). The chemical reactions taking place during the laser cutting of SS are more complex than the simple Fe → FeO reaction involved in the case of mild steel cutting. In this case, Fe, Cr, and Ni all oxidize simultaneously to form oxides according to the following reactions (Ref 7):

$$2Fe + 3/2\ O_2 \rightarrow Fe_2O_3 \qquad \Delta H = -826.72\ kJ/mol \text{ at } 2000\ K$$

$$2Cr + 3/2\ O_2 \rightarrow Cr_2O_3 \qquad \Delta H = -1163.67\ kJ/mol \text{ at } 2000\ K$$

$$Ni + 1/2\ O_2 \rightarrow NiO \qquad \Delta H = -248.23\ kJ/mol \text{ at } 2000\ K$$

It has been estimated that the respective concentrations of Fe_2O_3, Cr_2O_3, and NiO in the ejected oxides are 78.4, 19.2, and

Harish Kumar, P. Ganesh, Rakesh Kaul, B. Tirumala Rao, Pragya Tiwari, and **A.K. Nath,** Industrial CO_2 Laser Section, Synchrotron Utilization Division, Centre for Advanced Technology, P.O.: CAT, Indore, 452 013 India; and **Ranjeet Brajpuriya** and **S.M. Chaudhari,** University Grants Commission-Department of Atomic Energy Consortium for Scientific Research, Indore, 452 017 India. Contact e-mail: rkaul@cat.ernet.in.

Table 1 Chemical composition of austenitic stainless steel sheet (in wt.%)

C	Cr	Ni	Mn	Si	Mo	Ti	S	P
0.032	19.37	8.84	1.66	0.50	0.33	0.003	0.021	0.037

Table 2 Parameters of laser cutting and laser welding

Laser cutting					
Average laser power	Frequency	Duty cycle	Cutting speed	Gas	Pressure
240 W	300 Hz	40%	5 mm/s	Oxygen	0.5 MPa
Laser welding					
Laser power		Welding speed		Shroud gas	
2.3 kW		12 mm/s		Ar	

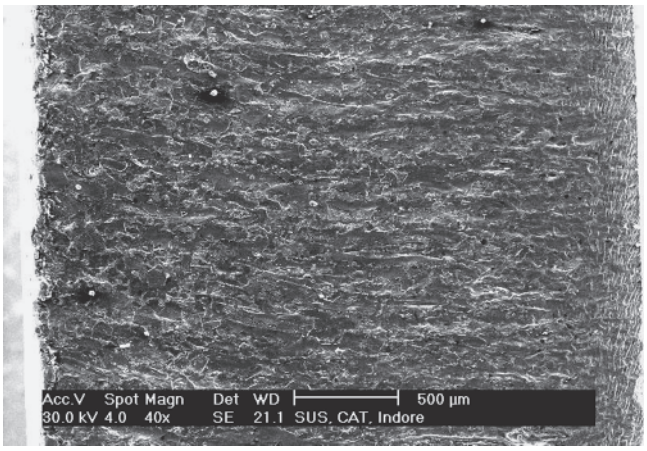

Fig. 1 Low-magnification view of the laser-cut surface of the SS sheet: (right) top edge; (left) bottom edge

2.4 mol%, respectively. However, the oxides constituted about 35.5 mol% of the total amount of the ejected material (Ref 8).

In the applications demanding the welding of laser-cut sheets, the weldability of the cut sheets is significantly influenced by thickness and the chemistry of the oxide layer left on the cut surface and by the roughness of the cut edge. An alternative for avoiding the oxide layer on the laser-cut edges is to use nitrogen as the assist gas. However, it results in a 30 to 60% reduction in the cutting speed (Ref 8, 9). Recent work carried out in the authors' laboratory demonstrated that the laser cutting of 1 mm thick silicon steel sheets in pulse mode (with oxygen as the cutting gas) yields improved quality of the cut surface compared to that produced by cutting in continuous wave (CW) mode (Ref 10).

3. Experimental

The current study was carried out on a 3 mm thick AISI 304 ASS sheet. Table 1 presents the chemical composition (in wt.%) of the SS sheet. Laser cutting was performed with an indigenously developed 2.5 kW transversely excited transverse flow CO_2 laser system (Ref 11). The laser can be operated in CW mode as well as in pulsed mode. The laser yields a maximum output power of 750 W in TEM_{01*} mode. TEM_{01*} mode was obtained by incorporating a suitable intracavity aperture. The plane-polarized LB coming out of the laser cavity was made circularly polarized with a phase-retarding mirror. The circularly polarized LB was subsequently focused with a meniscus zinc selenide (ZnSe) lens of 100 mm focal length. The focusing lens was housed in a coaxial copper nozzle (exit diameter 1.5 mm) through which the assist gas (oxygen) was blown. The focal point of the LB (typical spot diameter 200 µm) was located at a distance of about 1 mm from the nozzle tip. To control heat input during laser cutting, an important parameter controlling surface roughness and thickness of the oxide layer on the cut surface (which, in turn, affects the weldability of laser-cut sheets), the process was performed in pulsed mode.

The resultant laser-cut SS sheets were subsequently butt-welded with an indigenously developed 10 kW transversely excited transverse flow CW CO_2 laser (Ref 12, 13). The laser-welding setup consisted of the laser system integrated with a beam delivery system and a computer-controlled three-axis workstation. The raw LB, emanating out of the laser system, was folded with a 45° plane gold-coated copper mirror, and the folded LB was subsequently focused with a 100 mm focal length ZnSe lens. The focusing lens was mounted in a water-cooled copper nozzle. Autogenous laser welding was performed by scanning the sheet interface with the focused LB. During the course of the laser welding, argon gas was passed through the nozzle that served the dual purpose of protecting the expensive ZnSe lens from possible particulate emissions

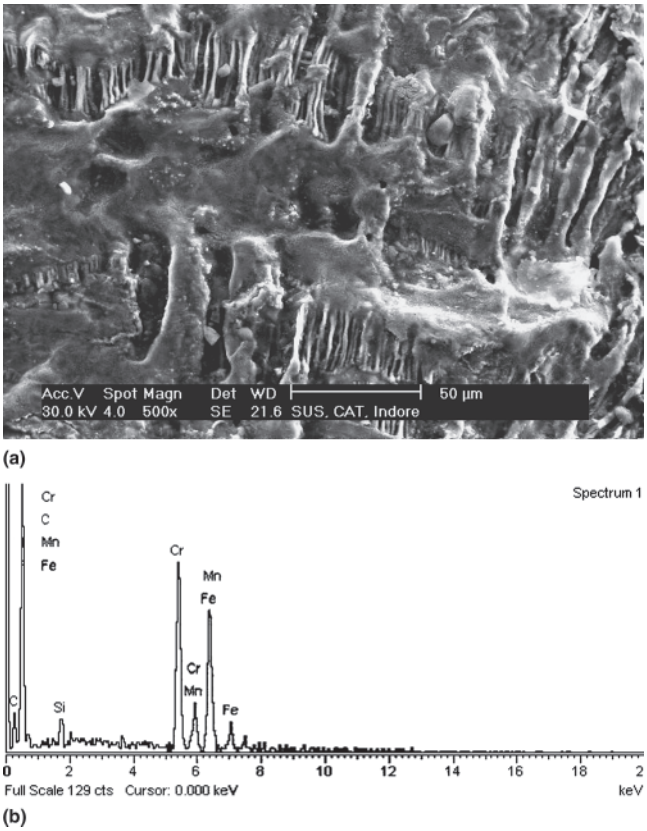

Fig. 2 (a) Parallel fibers near the top edge of the laser-cut surface. (b) The EDS spectrum of one of the fibers shown in (a)

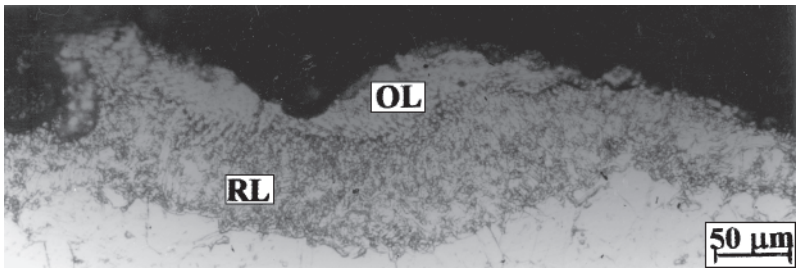

Fig. 3 Cross section of the laser-cut SS sheet. OL, oxide layer; RL, resolidified layer

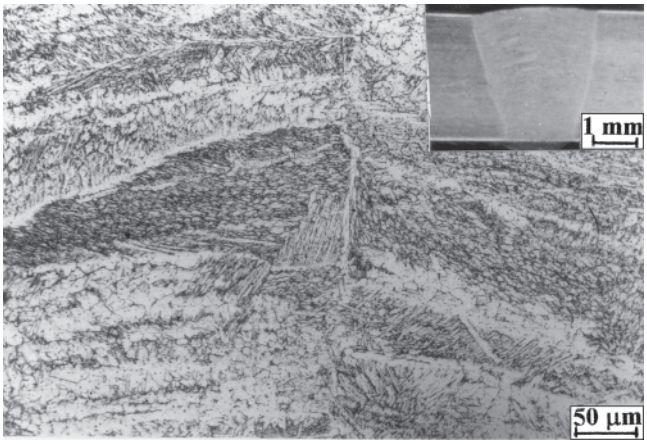

Fig. 4 The FZ microstructure of the LCW specimen. The inset shows the macroscopic view of the weldment.

from the substrate being welded as well as shielding the substrate being welded against oxidation. In addition to the laser welding of laser-cut SS sheets, some bead-on-plate laser-welded SS specimens were also prepared. Table 2 presents experimental parameters for laser cutting and laser welding.

Laser-cut, laser-welded, as well as base metal specimens were characterized by surface roughness measurement, x-ray photoelectron spectroscopy (XPS), optical microscopy, microhardness measurement, scanning electron microscopy (SEM), energy-dispersive spectroscopy (EDS), tensile testing of smooth and notched specimens, and guided bend test. In the subsequent part of the article, "laser-cut and laser-welded" specimens are referred to as LCW, "bead-on-plate laser-welded" specimens are referred to as LW, and 'base metal" specimens are referred as BM.

4. Results and Discussion

4.1 Surface Roughness Measurement

The surface roughness measurement of (the cut surface of) laser-cut SS sheet measured with a Surtronic 3^+ (Taylor Hobson Ltd., UK) roughness tester revealed an Ra value of about 5 μm.

4.2 Scanning Electron Microscopy Examination of Laser-Cut Surface

Laser-cut surfaces were not found to be associated with well-defined characteristic "striations." Figure 1 presents a low-magnification photomicrograph of the laser-cut surface. Except for a small zone near the top edge, which is shown on the right side of Fig. 1, most of the cut surface was largely featureless. Near the top edge, the cut surface carried regular pockets of parallel fibers, as shown in Fig. 2(a). The EDS analysis identified the fibers as Cr-rich oxides, as shown in Fig. 2(b). A few gas porosities were also noticed near the bottom edge of the laser-cut surface.

It is believed that parallel fibers represent chromium-rich oxides that are formed on the elongated inclusions near the top surface where heat input was too low to facilitate the efficient ejection of refractory chromium oxide. The mechanism involved during the initial part of laser cutting is the formation of a depressed melt pool under the influence of gas jet. The cavity so formed rapidly deepens and results in a keyhole. At this stage, the mechanism of material removal involves material evaporation, which proceeds until the LB moves past the region under consideration. Due to the very high temperatures involved during the intermediary stage of laser cutting, chromium oxide particles were not found in this region. In the final stage of laser cutting, the molten metal is dragged out of the cut front by the force of the assist gas (Ref 14).

4.3 Metallographic Examination

The laser cutting of the ASS sheet produced a kerf width of 350 to 400 μm. Metallographic examination of the transverse cross sections of the laser-cut specimens revealed a thin-melted and resolidified layer below the cut edge. The layer was covered with a thin layer of oxide. The average thickness of the melted and resolidified layer registered an increase toward the bottom edge of the SS sheet. The thickness of the melted and resolidified layer was 10 to 40 μm near the top edge, while it increased to 50 to 80 μm near the bottom edge of the laser-cut sheet. Figure 3 presents a magnified view of the transverse cross section of the laser-cut SS sheet specimen.

Both kinds of laser weldments (i.e., LCW and LW) exhibited full penetration. No defects were found in the weldments. The fusion zone (FZ) of the two welds exhibited the primary ferrite mode of solidification. Figure 4 presents the FZ microstructure of the LCW specimen. Figure 4 carries the macroscopic view of the laser weldment in the inset. A closer look at the FZ microstructure revealed a largely uniform dispersion of fine inclusions, as shown in Fig. 5(a). The EDS analysis of the inclusions confirmed the presence of C and O along with Fe, Cr, Ni, and Mn, as shown in Fig. 5(b). It is believed that the inclusions were the result of the oxide layer present on the laser-cut surfaces. Such inclusions were not found in the FZ of the LW specimen. Figure 6 presents the FZ microstructure of the LW specimen.

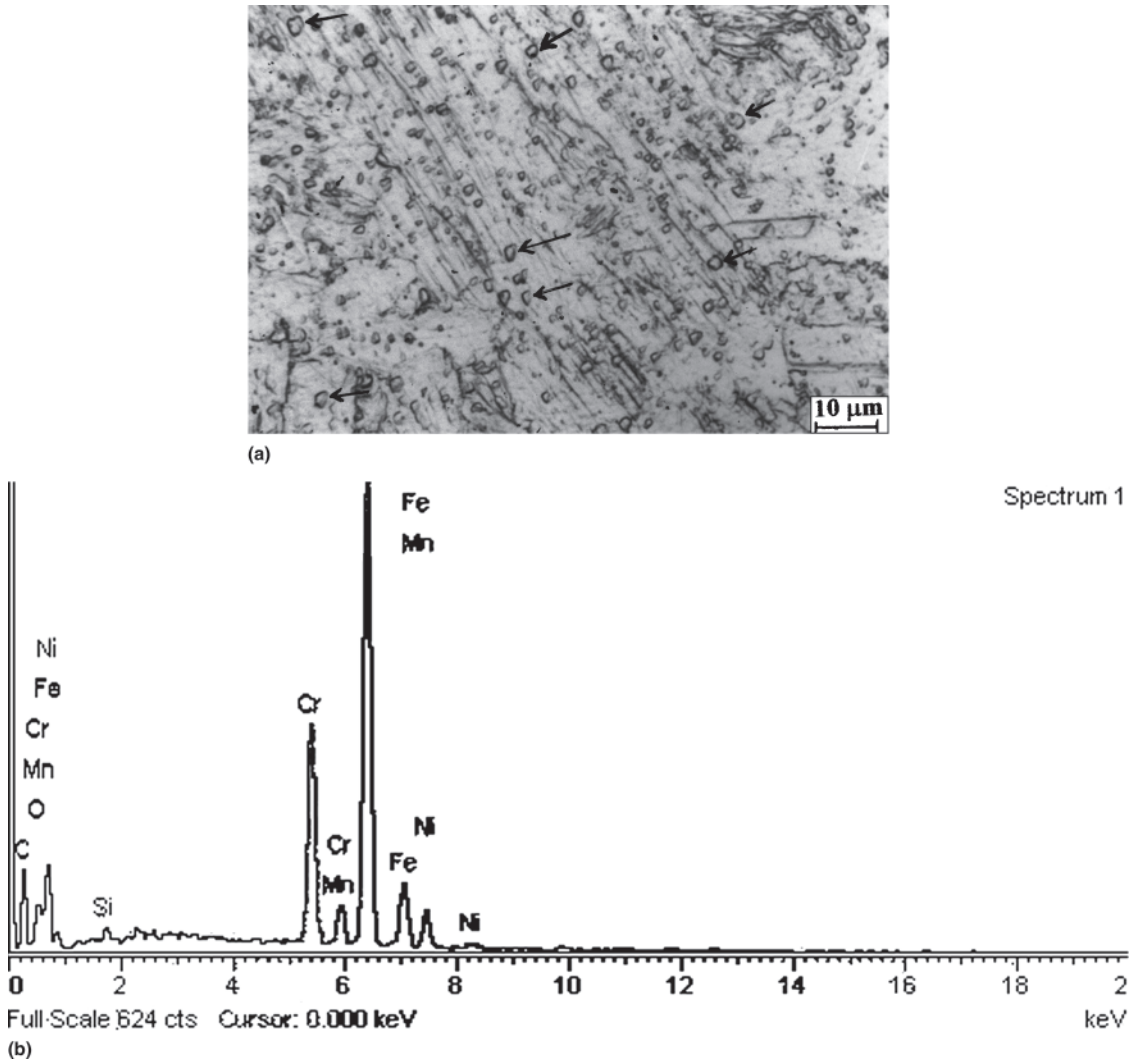

Fig. 5 (a) The uniformly dispersed fine inclusions (marked with arrows) in the FZ of the LCW specimen. (b) The EDS spectrum of one of the fine inclusions in the FZ of the LCW specimen

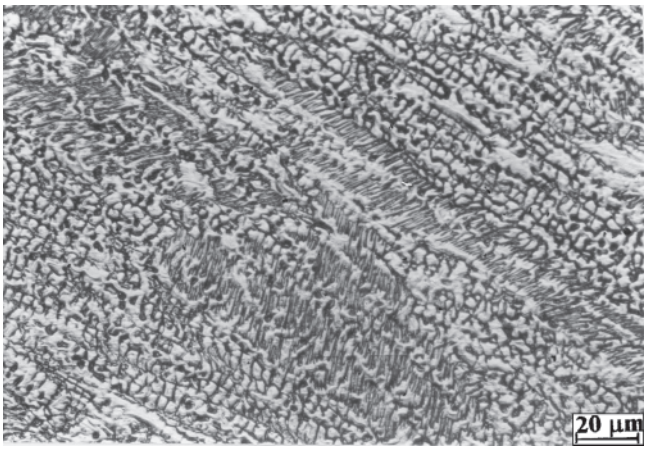

Fig. 6 The FZ microstructure of the LW specimen

4.4 Microhardness Measurement

Microhardness measurements (load 0.981 N) were performed on the transverse cross section of laser-welded (i.e., LW and LCW) specimens. The measurements revealed that in comparison to the largely uniform microhardness profile across the LW weldment, the LCW specimen exhibited a relatively higher microhardness (213–271 VHN) in the FZ with respect to the base metal (204–230 VHN). Figure 7 presents microhardness profiles across the cross sections of laser weldments.

4.5 X-Ray Photoelectron Spectroscopy

The XPS measurements were performed on an as-laser-cut surface and the FZ of the LCW specimen using workstation of photo-electron spectroscopy beam line installed at INDUS-1, a synchrotron radiation source at the Center for Advanced Technology, Indore, India. The sample for the FZ of the LCW specimen was extracted by taking out a thin slice of material along the longitudinal cross section of the weld. The specimens for XPS were prepared by the side-by-side placement of four numbers of the concerned pieces to present a surface area of 10 × 10 mm. All of the measurements were made by using MgKα radiation having 1253.6 eV photon energy. At the pass energy of 50 eV, the measured resolution was better than 0.8 eV. The binding energies (BEs) of the observed peaks were determined using an internal reference (defined as C-1s) at 284.7 eV and

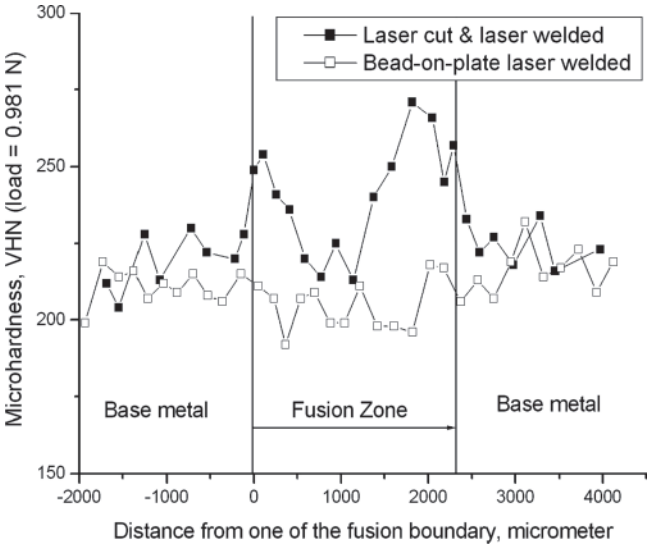

Fig. 7 Microhardness profile across the cross section of laser-welded specimens

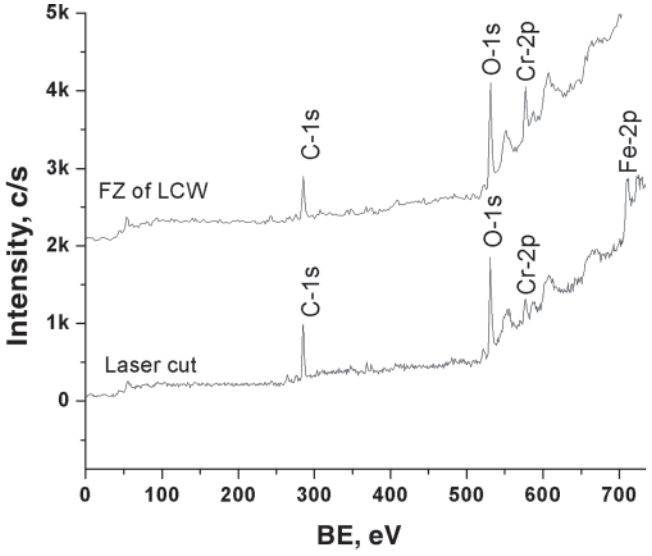

Fig. 8 The XPS survey scans of the laser-cut surface and FZ of the LCW specimen

external references as Au-$4f_{7/2}$ and Au-$4f_{5/2}$ at 83.8 eV and 87.5 eV, respectively. Before taking test measurements, the specimens were sputtered with Ar^+ ions for 10 min to remove surface contamination. The survey scans of both of the specimens are shown in Fig. 8. The survey scan exhibited intense peaks of C-1s (BE 285.2 eV) and O-1s (BE 530.7 eV). In addition, smaller peaks of Fe 2p and Cr 2p were also detected in the survey scan. The narrow scans of O-1s and C-1s peaks were also separately recorded, and are shown in Fig. 9 and 10, respectively. Figure 9(a) and (b) present the detailed XPS spectra of O-1s for the laser-cut specimen as well as the FZ of the LCW specimen. The observed peaks were broad and were deconvoluted by using standard XPSpeak41 software (Ref. 15). The spectra were resolved into their components after subtracting the Shirley background (Ref 16). The O-1s spectrum for the laser-cut surface was resolved in two components: Cr_2O_3 and Fe_2O_3. On the basis of the relative area under the peaks, the

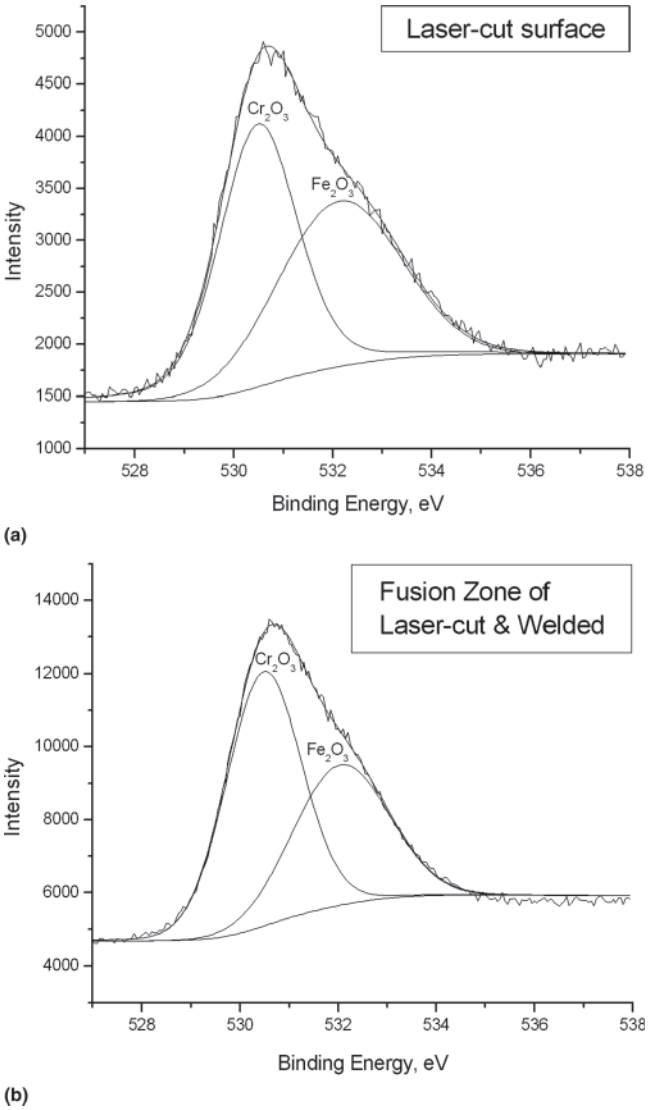

Fig. 9 (a) Detailed XPS spectrum of O-1s signals of the laser-cut SS surface. (b) Detailed XPS spectrum of O-1s signals of the FZ of the LCW specimen

proportion of Fe_2O_3 and Cr_2O_3 was found to be 47:53 (atomic). This value matches quite well with the 48:52 (atomic) figure reported by Powell and Menzies (Ref 7). The observed O-1s spectrum for the FZ of the LCW specimen was quite similar to that of the laser-cut surface, but with a marginally different Fe_2O_3-to-Cr_2O_3 ratio of 41:59 (atomic). The similar natures of the O-1s spectra of the laser-cut surface and the FZ of the LCW specimen indicate that the nature of the oxides remained unchanged during the laser welding of laser-cut sheets. On the basis of the results of the metallographic examination and the XPS, it is evident that during the course of laser welding the surface oxides were significantly refined and dispersed in the FZ.

Figure 10 presents C-1s spectra for the two specimens analyzed. The peak position in the two spectra matched well with that of C-1s, indicating that the C was largely present in the elemental form.

4.6 Tensile Test

Laser-welded tensile test specimens were fabricated as per the Boiler and Pressure Vessel Code (section VIII) (Ref 17).

The test specimen carried laser welds in the center of its gage length. In addition to the laser-welded specimens (LCW and LW), the tensile tests were also performed on BM specimens of the same dimensions. All of the specimens exhibited largely similar tensile and yield strength values, although the LCW specimens exhibited lower ductility than the BM and LW specimens. All laser-welded specimens suffered failure in the FZ. The results of tensile tests are summarized in Table 3.

The SEM fractographic examination of the failed specimens revealed dimpled surfaces reflecting the ductile nature of the failure. The average size of the dimples was significantly coarser in the BM specimen than that in laser-welded specimens. Figure 11 compares the fractographic features of BM and LCW specimens at the same magnification. Ductile failure of metals/alloys involves the formation of microvoids around inclusions, their growth, and finally their coalescence to bring about fracture, giving rise to the dimpled nature of the fractured surface. Microvoids are formed as a result of particle-matrix decohesion or the cracking of second-phase particles. The process of microvoid growth involves considerable localized plastic deformation and requires the expenditure of large amounts of energy (Ref 18). Therefore, finer dimples in laser-welded specimens are indicative of lower ductility of these specimens with respect to BM.

4.7 Notch Tensile Test

Notch tensile tests were performed with the objective of comparing the notch sensitivity of the FZ of LCW specimens with respect to BM. Figure 12 presents the drawing of the test specimen. Notch tensile testing of LCW and BM specimens magnified the difference between their ductility. Careful observation of the specimens during the course of testing revealed that in BM specimens gross plastic deformation was introduced (causing crack tip blunting) at an earlier stage than that in the LCW specimens. In these specimens, the crack extended with two zones of plastic deformation (appearing in the form of relief on the surface of the specimens under testing), inclined at about 45° with respect to the direction of crack extension. On the other hand, in LCW specimens the inclination of the plastically deformed zones (with respect to the direction of crack extension), which developed ahead of the crack tip, was much lower. The BM specimens exhibited greater notch tensile strength and ductility than those of the LCW

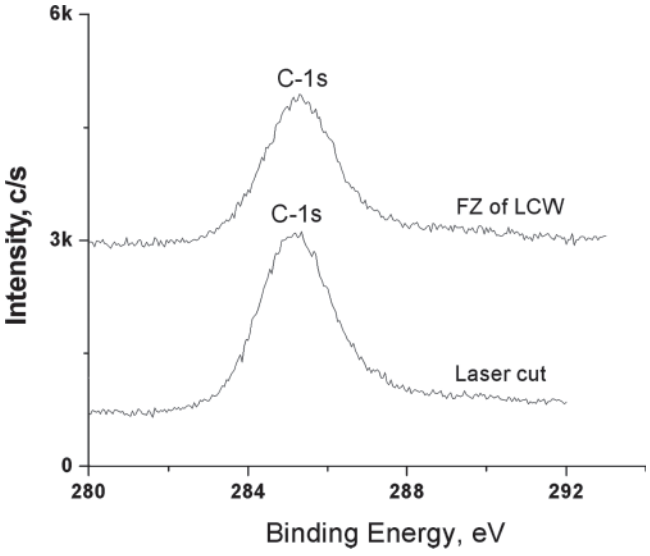

Fig. 10 Detailed XPS spectra of C-1s signals of the laser-cut SS surface and the FZ of the LCW specimen

Table 3 Results of tensile testing

Specimen	Yield strength, MPa	Tensile strength, MPa	Elongation (gauge length = 15 mm), %	Failure location
Unnotched				
BM	346	656	75	…
	305	631	68	…
	304	630	69	…
LCW	353	631	56.5	Weld
	356	637	43.5	Weld
	335	619	49.5	Weld
	355	635	55	Weld
LW	345	634	59	Weld
	325	620	62	Weld
	349	621	65.6	Weld

Specimen	Notch tensile strength, MPa	Reduction in area, %	Failure location	NSR
Notched				
BM	564	62	…	0.86-0.90
	562	56	…	
LCW	462	29	Weld	0.71-0.75
	454	32	Weld	

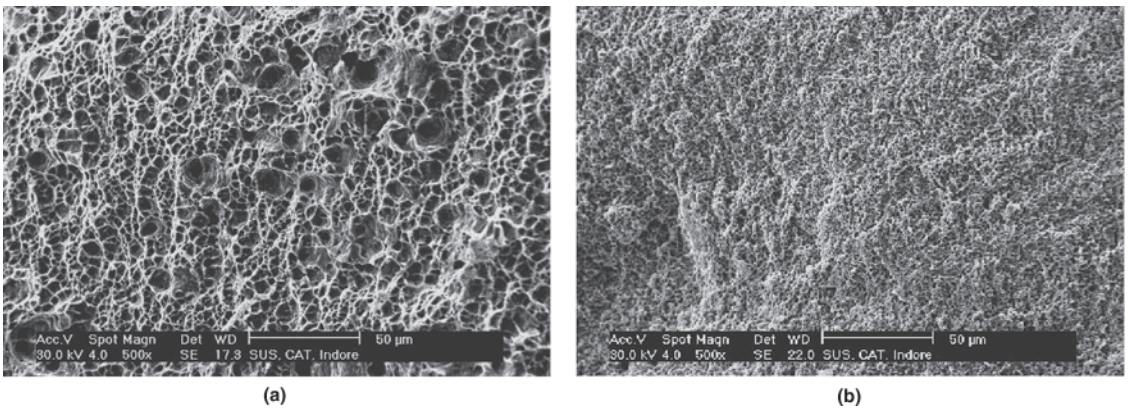

Fig. 11 Comparison of dimpled fracture surfaces of tensile tested (a) BM specimen and (b) LCW specimen

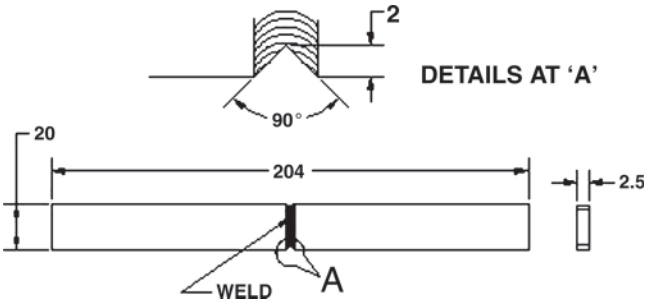

Fig. 12 Drawing of a notch tensile test specimen

specimens. The LCW specimens displayed a lower notch strength ratio (NSR; 0.71–0.75) than that of BM specimens (0.86–0.9). The NSR is defined as the ratio of the notch tensile strength to the tensile strength of the unnotched specimen (Ref 19). The results of notch tensile tests are summarized in Table 3.

The SEM fractographic examination of notch-tensile tested LCW and BM specimens revealed sharp differences in their surface morphologies near the notch root. In the BM specimen, a narrow "smooth zone" was noticed at the roots of the two notches, as shown in Fig. 13(a). The smooth zones were inclined with respect to the rest of the fractured surface and were associated with elongated dimples (Fig. 13b), indicating the influence of shear stresses near the notch root (Ref 20). The rest of the fractured surface exhibited coarse equiaxed dimples. On the other hand, in LCW specimens, no such smooth zones were noticed at the roots of either of the two notches. Figure 14 presents a low-magnification SEM fractograph of the LCW specimen showing the absence of the smooth zone near the notch root. The whole fractured surface of the specimen displayed finer equiaxed dimples, signifying a lower degree of plastic deformation (preceding failure) with respect to the BM specimen. A metallographic examination of the top surface of the fractured BM specimen exhibited a fine "V-notch" region at the root of the machined notch, which corresponded to the smooth zone noticed on the fractured surface, as shown in Fig. 13(a). The material around the V-notch region exhibited signatures of plastic deformation, as shown in Fig. 15. The development of a fine V-notch region during the initial process of failure signifies fracture along planes at 45° to the stress-axis. During the subsequent period of the failure, the specimen fractured along the planes normal to the direction of applied stress. In contrast to the BM specimens, no such features were noticed in the LCW specimens.

Notch tensile tests demonstrated that, in contrast to LCW specimens, BM specimens developed plane stress conditions at the notch-root, which facilitated deformation on the planes of maximum shear stress (at 45° to the stress-axis), causing blunting of the notch root (Ref 20). The argument is supported by the development of fine V-notch region (with signs of plastic deformation around it) at the root of the notch. The relatively lower value of the NSR of LCW specimens (with respect to that of BM specimens) also indicates that due to the limited ability of the FZ of the LCW specimens to plastically deform and blunt the crack tip, stress concentration effects were more dominant and brought about the failure of these specimens at lower applied stress. This means higher notch sensitivity of the FZ of LCW with respect to BM (Ref 20). The higher notch sensitivity and lower ductility of the FZ of the LCW specimens

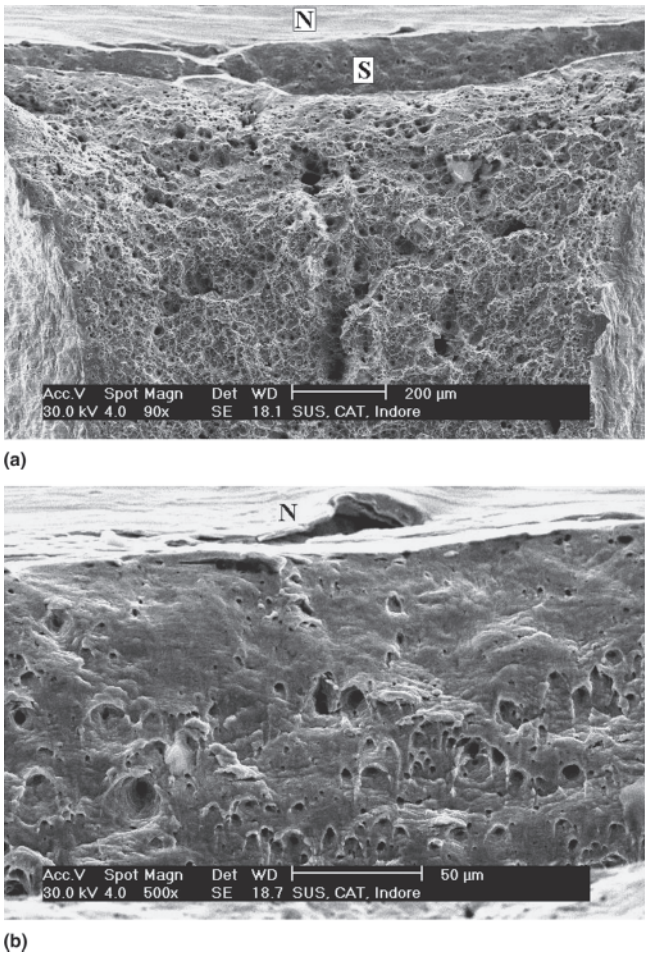

Fig. 13 (a) Low-magnification view of the fracture surface of notch tensile-tested BM specimen near the notch root. Note a thin smooth zone near the notch root. (b) Elongated dimples on the smooth zone shown in (a). S, smooth zone; N, notch root

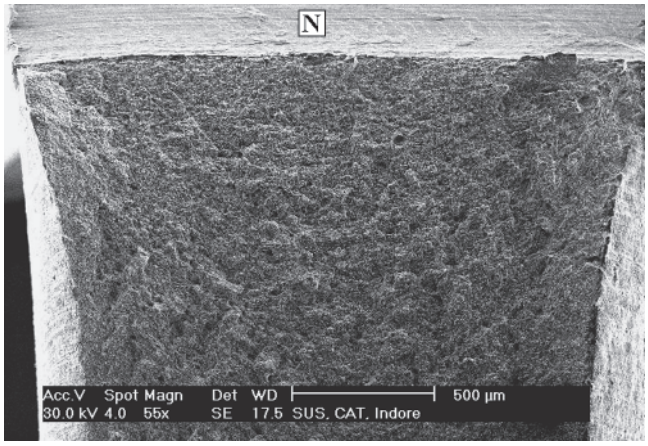

Fig. 14 Low-magnification view of the fracture surface of notch tensile-tested LCW specimen near the notch root (N)

with respect to BM is attributed to the presence of finely dispersed oxide inclusions in the FZ of LCW specimens, which brought about an increase in the hardness of the material (although the rise is not very large) and suppressed plastic deformation at the crack tip.

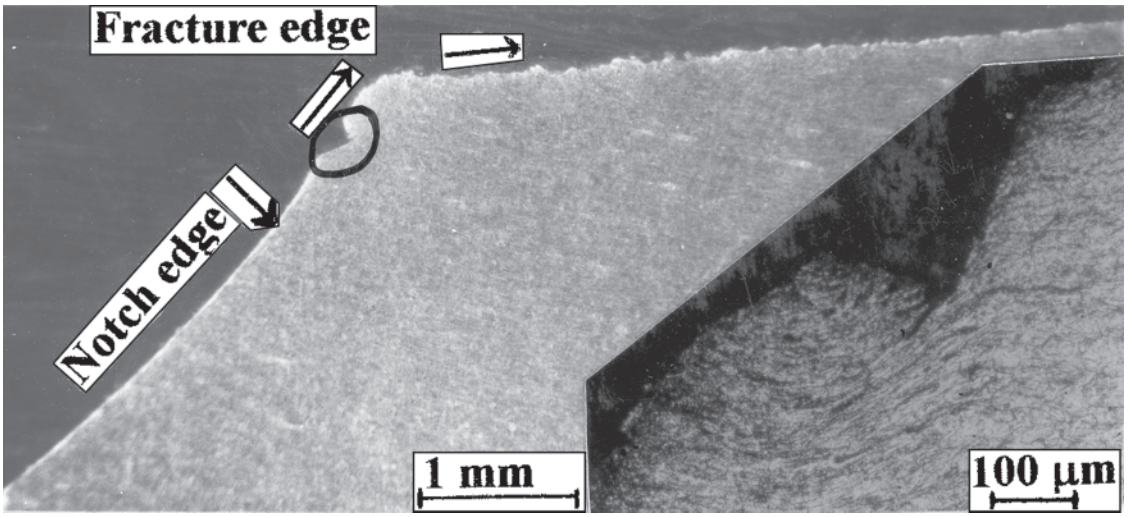

Fig. 15 Top surface of notch tensile-tested BM specimen showing a fine V-notch (encircled) at the root of the machined notch. The inset shows signs of plastic deformation around the V-notch region.

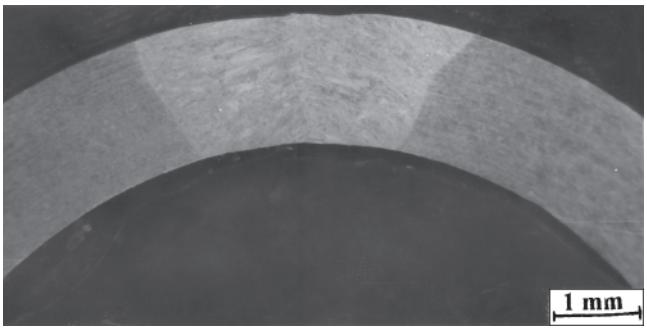

Fig. 16 Transverse cross section of guided bend-tested LCW specimen

4.8 Guided Bend Test

The LCW specimens were also subjected to a transverse-face guided bend test conducted as per ASTM E 190-92 (Ref 21). Three of these specimens were slowly bent to 180° in such a way that the top weld face became the convex surface. A macroscopic examination of the convex surface of the bent specimens revealed a smooth crack-free surface. A metallographic examination of the transverse cross section of the bent specimens did not reveal any defects. Figure 16 presents a magnified view of the cross section of the bent LCW specimen.

5. Conclusions

The results of the study demonstrated that laser welding can produce sound butt welds between 3 mm thick AISI 304 SS sheets that have been laser-cut using oxygen as an assist gas. For the improved weldability of laser-cut sheets, laser cutting was performed in pulsed mode with controlled heat input. The welds of the resultant laser-cut sheets possessed largely similar ultimate tensile strength values as that of the base metal. The relatively lower ductility of the LCW specimen with respect to the BM and LW specimens is attributed to finely dispersed oxide inclusions, arising out of the oxide layer present on the laser-cut surface in the FZ of LCW weldment. These welds also carried higher notch sensitivity than the base metal. However, laser-cut and laser-welded specimens were still ductile enough to pass the guided bend test.

Acknowledgments

The authors thank Dr. D.M. Phase and Mr. Vinay Ahire of the University Grants Commission-Department of Atomic Energy Consortium for Scientific Research, Indore, for EDS analysis. They also wish to thank Mr. Ram Nihal Ram, Mr. C.H. Prem Singh, and Mr. Anil Adbol for their assistance at various stages of this work.

References

1. S.E. Nielsen and G. Broden, Improved Weldability of Stainless Steel Cut by Laser, Power Beam Technology, J.D. Russell, Ed., September 10-12, 1986 (Brighton, U.K.), The Welding Institute, Proc. Int. Conf., 1987, p 256-267
2. P.A. Molian, Laser Cutting of Thick Metallic Solids–A Reactive Gas Flow Approach, Laser Advanced Materials Processing (LAMP) (Osaka, Japan), High Temperature Society of Japan and Japan Laser Processing Society, Proc. Int. Conf., May 21-23, 1987, p 245-250
3. A. Ivarson, J. Powell, and C. Magnusson, The Role of Oxidation in Laser Cutting Stainless Steel and Mild Steel, *J. Laser Appl.,* 1991, 3 (3), p 41-45
4. A. Ivarson, J. Powell, and C. Magnusson, Laser Cutting of Steels: Analysis of the Particles Ejected during Laser Cutting, *Weld. World,* 1992, 30 (5/6), p 116 -125
5. W. Bolton, *Newnes Engineering Materials Pocket Book,* Heinemann-Newnes, 1990
6. W.M. Steen, *Laser Material Processing,* 2nd ed., Springer Verlag, 1998, p 115-116
7. J. Powell and I. Menzies, Metallurgical Implications of Laser Cutting Stainless Steel: Power Beam Technology, J.D. Russell, Ed., September 10-12, 1986 (Brighton, U.K.), The Welding Institute, Proc. Int. Conf. 1987, p 269-284
8. J. Powell, *CO_2 Laser Cutting,* Springer-Verlag, 1993, p 57-65, 211-215
9. J. Powell, *Laser Cutting of Metals: LIA Handbook of Laser Materials Processing,* 1st ed., J.F. Ready, Ed., Magnolia Publishing Inc., 2001, p 443-444
10. B.T. Rao, R.K. Sinha, and A.K. Nath, Optimization of Si-steel Cutting with CO_2 Laser, *Metals Mater. Proc.,* 2002, 14 (2), p 145-154
11. A.K. Nath, L. Abhinandan, and P. Choudhary, Characteristics of a

Pulse-sustained dc-Excited Transverse-Flow cw CO_2 Laser of 1.5-kW Output Power, *Opt. Eng.,* 1994, 33 (6), p 1889-1893
12. C.P. Paul, H. Kumar, T. Reghu, P. Bhargava, and A.K. Nath, Enhancement of Output Power in a 5 kW Transverse Flow CW CO_2 Laser, *DAE-BRNS National Laser Symposium,* Allied Publishers Ltd., December 2001, p 51-52
13. J. Khare, R. Sridhar, C.P. Paul, T. Reghu, and A.K. Nath, Operational Characteristics and Power Scaling of a Transverse Flow Transversely Excited CW CO_2 Laser, *Pramana,* 2003, 60 (1), p 99-107
14. A. Bharti and R. Sivakumar, The Mechanism of Material Removal in Laser Fusion Cutting, *Lasers Eng.,* 1996, 5 (2), p 87-105
15. XPS analysis data fitting shareware program; www.icg.nsrrc.org.tw
16. D.A. Shirley, High-resolution X-Ray Photoemission Spectrum of the Valence Bands of Gold, *Phys. Rev. B: Condens. Matter,* 1972, 5, p 4709-4714
17. *Boiler and Pressure Vessel Code, Section IX: Welding and Brazing Qualification,* ASME, 1986, p QW-151, QW-462
18. J.R. Davis, Ed., *ASM Handbook*, 2nd ed. ASM International, 1998, p 1214
19. G.E. Dieter, *Mechanical Metallurgy,* McGraw-Hill, 1988, p 314-316
20. R.W. Hertzberg, *Deformation and Fracture Mechanics of Engineering Materials*, 4th ed., John Wiley & Sons, Inc., 1996, p 295-297, 342-345
21. 'Standard Method for Guided Bend Test for Ductility of Welds," E 190-92, *Annual Book of ASTM Standards,* ASTM, 1992